

Chapter 14

Modeling and Optimization of Thermoelectric Modules for Radiant Heat Recovery



Je-Hyeong Bahk and Kazuaki Yazawa

Abstract In this chapter, we present a detailed methodology for modeling and optimization of multielement thermoelectric (TE) power generation modules for radiant heat recovery application. Radiative heat sources such as concentrated solar irradiation and radiation from hot steel casting in steel production processes are considered as examples in this application. Large temperature difference across TE elements is typically created by the strong radiation heat transfer due to high-temperature source. Therefore, temperature-dependent TE material properties are considered for accurate simulation. Iterative simulation method based on one-dimensional finite element method is employed to obtain the precise temperature profile along heat flow direction in each of TE elements. Optical parameters such as emissivity of gray surfaces and shape factors are considered to quantify the accurate heat input to estimate the conversion efficiency under various conditions of the source and TE module. Using fractional area coverage and thickness of element as key design parameters, the power output of the system is optimized with significantly reduced material mass in use, ultimately for enhanced power-per-cost.

Symbols Nomenclature

A_i – Surface area of object i ($i = 1$ for heat source, $i = 2$ for heat absorber) (m^2)
 A_n – Cross-sectional area of n -type TE element (m^2)
 A_p – Cross-sectional area of p -type TE element (m^2)
 A_{TE} – Cross-sectional area of TE element (m^2)
 A_{total} – Total area of TE module or total area of heat absorber (m^2)
 a – Area ratio of heat absorber area to heat source area
 C – Solar concentration (suns)

J.-H. Bahk (✉)

Department of Mechanical and Materials Engineering, University of Cincinnati,
Cincinnati, OH, USA

e-mail: bahkjg@uc.edu

K. Yazawa

Birck Nanotechnology Center, Purdue University, West Lafayette, IN, USA

- C_i – Radiation coefficient for blackbody emissive power from object i
 E_{bi} – Blackbody emissive power of object i (W/m^2)
 $E_{b\lambda}(\lambda)$ – Monochromatic blackbody emissive power as a function of wavelength (W/m^3)
 F – Fill factor of TE module
 F_{ij} – Radiation shape factor from object i to object j
 G – Solar irradiation (W/m^2)
 $G_\lambda(\lambda)$ – Monochromatic irradiation as a function of wavelength (W/m^3)
 h_{conv} – Convection heat transfer coefficient ($\text{W} \times \text{m}^{-2} \times \text{K}$)
 I – Electrical current (A)
 J_i – Radiosity of object i (W/m^2)
 K_i – Thermal conductance of i th segment (W/K)
 κ_{filler} – Thermal conductivity of TE module filler ($\text{W} \times \text{m}^{-1} \times \text{K}^{-1}$)
 L – Length or distance (m)
 L_{slab} – Distance between hot steel slab and TE module (m)
 L_{TE} – Thickness of TE element (m)
 N – Number of segments in TE element
 $N_{\text{TE,pair}}$ – Number of TE element pairs in TE module
 P_{out} – Power output of TE module (W)
 $Q_{\text{conv,out}}$ – Heat loss by convection from hot side of TE module (W)
 $Q_{\text{in},n}$ – Heat input to n -type element (W)
 $Q_{\text{in},p}$ – Heat input to p -type element (W)
 $Q_{\text{in,TE}}$ – Total heat input to all TE elements (W)
 $Q_{\text{in,system}}$ – Total system heat input before heat losses (W)
 Q_{J_i} – Joule heat at i th node (W)
 Q_{K_i} – Incoming conduction heat to i th node (W)
 Q_{lateral} – Lateral heat exchange in hot-side plate between a pair of TE elements (W)
 Q_{P_i} – Peltier heat at i th node (W)
 $Q_{\text{rad,in}}$ – Radiant heat input to TE module (W)
 $Q_{\text{rad,out}}$ – Heat loss by radiation from hot side of TE module (W)
 R_c – Contact resistance at junction between electrode and TE element (Ohm)
 R_{el} – Electrical resistance of electrode (Ohm)
 R_i – Electrical resistance of i th segment (Ohm)
 R_{ij} – Radiation space resistance from object i to object j (m^{-2})
 R_{int} – Internal resistance of TE module (Ohm)
 R_L – Load resistance (Ohm)
 R_{si} – Radiation surface resistance of object i (m^{-2})
 S_i – Average Seebeck coefficient in i th segment (V/K)
 T – Temperature (K)
 T_{amb} – Ambient temperature (K)
 T_{bot} – Bottom-side temperature of TE module (K)
 T_C – Cold-side temperature of TE element (K)
 T_H – Hot-side temperature of TE element (K)
 T_i – Temperature of i th node or i th object (K)

- T_{top} – Topside temperature of TE module or temperature of heat absorber (K)
 V_{OC} – Total open-circuit voltage from TE module (V)
 V_{OC_i} – Open-circuit voltage from i th segment (V)
 V_{out} – Total output voltage to the load (V)
 w – Width (m)
 w_{slab} – Width of hot steel slab
 ZT – Thermoelectric figure-of-merit of TE material
 α – Absorptivity of heat absorber
 $\alpha_\lambda(\lambda)$ – Monochromatic absorptivity as a function of wavelength
 $\varepsilon_i(\lambda)$ – Monochromatic emissivity as a function of wavelength
 ε_i – Emissivity of object i ($i = 1$ for heat source, $i = 2$ for heat absorber)
 η – Efficiency of TE system
 η_{TE} – Efficiency of TE module
 κ_i – Average thermal conductivity in i th segment ($\text{W} \times \text{m}^{-1} \times \text{K}^{-1}$)
 λ – Wavelength of radiation (m)
 ρ_i – Reflectivity of object i ($i = 1$ for heat source, $i = 2$ for heat absorber)
 σ_{SB} – Stefan-Boltzmann constant ($=5.670 \times 10^{-8} \text{ W} \times \text{m}^{-2} \times \text{K}^{-4}$)
 σ_i – Average electrical conductivity in i th segment (S/m)
 τ – Transmissivity of solar concentrator lens
 ψ_h – Conductive heat transfer coefficient of hot-side plate (Wm^{-2}K)
 ψ_c – Conductive heat transfer coefficient of cold-side plate (Wm^{-2}K)

14.1 Introduction

Since the dawn of modern thermoelectrics in the 1950s, numerous applications have emerged and flourished for energy conversion with thermoelectric devices [1, 2]. Examples include radioisotope thermoelectric generators (RITEGs) for deep space missions [3], vehicle exhaust waste heat recovery with TEGs [4], compact refrigeration [5], portable energy harvesters, [6] and self-powered sensor nodes [7]. Recently, wearable energy harvesting from human body heat has been gaining great attention as a new application for thermoelectrics in this smart wearable electronics era [8]. Most of these applications, however, rely on the physical attachment of TE module onto the heat source surface in order to promote efficient heat transfer from the source to TE module by conduction. Unfortunately, radiant heat conversion by thermoelectrics has not been investigated as much thus far.

Radiant heat is transferred by electromagnetic radiation in a free space with no medium involved. Radiation heat transfer is everywhere so long as there is a temperature difference between the objects. Although it is usually small at low- to medium-temperature ranges below ~ 600 K, radiative emissive power increases rapidly with increasing temperature, following the fourth power of absolute temperature ($\sim T^4$), thus potentially useful as a strong heat source for thermoelectric power generation in high-temperature industrial applications. Recent advances in

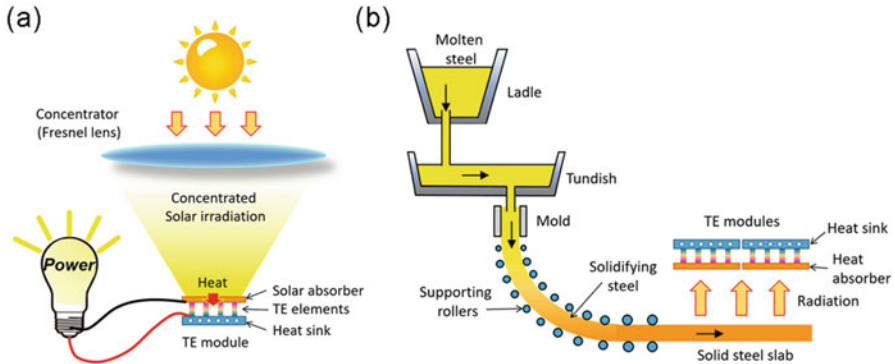


Fig. 14.1 Schematics of thermoelectric radiant heat recovery system (a) in concentrating solar irradiation and (b) in industrial hot steel casting processes

development of low-cost, high-efficiency optical concentrators such as parabolic mirrors or Fresnel lenses enable high concentration of radiation to magnify the heat flux to TE module for enhanced conversion efficiency and power generation with minimal cost added [9, 10]. Furthermore, radiant heat is a noncontact heat source that can be harvested by TEG from a distance. TE module would impose minimal impacts on the performance of the source system due to its noncontact nature. Additional contact resistances and interface damages/cracks due to thermal stresses that are commonly observed in physically attached TE modules [11] would not be an issue in radiant heat recovery TE system.

One of the most important and abundant radiant heat is solar irradiation. Solar energy is sustainable and easily accessible for energy harvesting. When solar energy is absorbed by solar absorber and converted to heat, this heat can then be converted to electricity by TEG [12, 13]. This technology is known as so-called solar thermoelectric technology. Recently, good reviews on solar thermoelectric technology have been published [14, 15]. A schematic of concentrated solar thermoelectric system is shown in Fig. 14.1a. Solar radiation is typically concentrated into a smaller area covered by TEG module as shown in the schematic in order to increase the operating temperature and thus the conversion efficiency. A heat sink might be necessary to keep sufficiently high the temperature difference between hot and cold sides of TEG module, which, however, consumes power for its operation and thus reduces in system efficiency. Recently, peak system efficiency of 7.4% has been demonstrated for concentrating solar TEG made of segmented TE elements in high-vacuum operation [16]. This result suggests a great potential of solar thermoelectric systems to become a promising alternative solar energy technology.

Another important industrial application with strong radiant heat available for harvesting is found in hot steel casting process in steel manufacturing [17, 18]. Steel manufacturing processes consume a huge amount of electric power. The autonomous operation of the processing lines, e.g., hot rolling mills or continuous casting lines, requires hundreds of sensors such as hot metal detectors, light barrier switches,

and proximity switches to ensure reliability and robustness of production [19]. TEG module capable of generating power out of the heat radiated from hot steel slabs, as schematically shown in Fig. 14.1b, can in turn power many such sensors without resorting to the grid power. This will ensure lower electrical power requirement, higher utilization of input power, and more environment-friendly operation.

Since very large temperature difference ~ 200 K or higher is typically applied to TEG module in radiant heat recovery applications, variations of material properties with temperature over the wide temperature range are critical in module performance. Unfortunately, the effects of temperature-dependent material properties have not been much studied nor accurately accounted for in module simulations in literature so far. A good review of thermoelectric simulation has been published in [20]. Also, temperature boundary conditions are typically used for module simulations [21, 22], e.g., constant topside temperature, but these assumptions are no longer valid in radiant heat recovery applications because the boundary temperatures are not fixed but rather determined after solving for the entire temperature profile across TE module with accurate quantification of heat inputs and losses. For precise performance prediction and module optimization, simulation tool is essential that is capable of accounting for all these effects and unique features. We have published our simulation tool for solar TE systems on nanoHUB.org for public use [23].

In this chapter, we present our simulation methodology and module optimization for TE systems for radiant heat recovery. We employ iterative, one-dimensional finite element methods to accurately determine distributions of temperature along individual TE elements with accounting of temperature-dependent material properties. Heat inputs from the radiative heat exchanges between the objects involved and heat losses due to convection and back radiation, as well as TE filler effects, are quantified for accurate simulation. Our detailed module simulation methodology will be discussed in Sect. 14.2. In Sects. 14.3 and 14.4, we will present the simulation results for concentrating solar thermoelectric systems and hot steel casting application, respectively. We will identify optimal module designs and impacts of various design parameters on power output and efficiency, for these two applications. Like any other renewable energy technologies, presented simulations could be helpful for estimation of power-per-cost value, which can only be achieved by careful design of TE module and whole system [24]. We will provide guidelines to achieve high power-per-cost in these applications.

14.2 Theory and Simulation Methodology

Figure 14.2 shows a schematic of multielement TE module for radiant heat recovery. The top surface of TE module is made of heat absorber, i.e., with high emissivity surface, which efficiently absorbs $Q_{\text{rad,in}}$ from heat source located with a certain distance. Concentration of heat is possible using optical concentrators as mentioned earlier before the heat reaches the top surface of TE module to increase $Q_{\text{rad,in}}$ by factor of concentration C . Some portion of $Q_{\text{rad,in}}$ is dissipated to ambient at the top

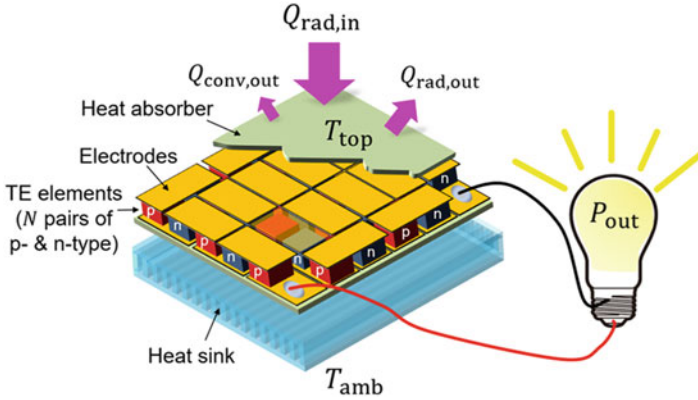


Fig. 14.2 Schematic of multielement TE module for radiant heat recovery. Radiant heat input $Q_{\text{rad, in}}$ and heat losses by radiation $Q_{\text{rad, out}}$ and by air convection $Q_{\text{conv, out}}$ at the topside (heat absorber side) of TE module are displayed. No vacuum enclosure is assumed

surface via back radiation $Q_{\text{rad, out}}$ and air convection $Q_{\text{conv, out}}$. The whole TE module can be surrounded by high-vacuum enclosure to minimize $Q_{\text{conv, out}}$ loss. In this work, however, we assume ambient air surroundings to eliminate the additional installation and maintenance costs for vacuum enclosure. The convection loss can still be much smaller than other parasitic heat losses, so air surrounding may be acceptable without much performance reduction. The remaining heat will pass through TE elements, with some losses by conduction through the air or filler material in the spacing between TE elements, and be partially converted by TE effects to electric power P_{out} , which is delivered to the load. The rest of the heat is then dissipated to ambient by the heat sink at the bottom of the system. In the next subsection, we will discuss the heat transfer model to determine the heat inputs and losses at the topside.

14.2.1 Heat Transfer Model

In solar TE system, in which the heat source is the sun, $Q_{\text{rad, in}}$ is given by:

$$Q_{\text{rad, in}} = GC\tau\alpha A_{\text{total}}, \quad (14.1)$$

where G is solar irradiation power density in W/m^2 ; C is solar concentration defined as the ratio of solar concentrator area to TE absorber area in the unit of suns; τ is the transmissivity of solar concentrator lens or the reflectivity if concentrator is a mirror type; α is the absorptivity of solar absorber equipped at the top surface of TE module; and A_{total} is the total area of TE absorber plate. The absorptivity α is a weighted average of monochromatic absorptivity $\alpha_{\lambda}(\lambda)$ of the absorber with monochromatic

solar irradiation $G_\lambda(\lambda)$ as the weighting factor over the entire wavelength range given by [25]:

$$\alpha = \frac{\int_0^\infty \alpha_\lambda(\lambda) G_\lambda(\lambda) d\lambda}{\int_0^\infty G_\lambda(\lambda) d\lambda}, \quad (14.2)$$

The heat loss by radiation from TE absorber plate occurs because there is radiation exchange between the plate surface and the surroundings, which is given by:

$$Q_{\text{rad, out}} = \varepsilon \sigma_{\text{SB}} A_{\text{total}} \left(T_{\text{top}}^4 - T_{\text{amb}}^4 \right), \quad (14.3)$$

where ε is the emissivity of TE absorber and σ_{SB} is Stefan-Boltzmann constant. Similarly, as the absorptivity, the emissivity is a weighted average of monochromatic emissivity $\varepsilon_\lambda(\lambda)$ of the surface with monochromatic blackbody emissive power $E_{b\lambda}(\lambda)$ as the weighting factor over the entire wavelength range at a given temperature T given by:

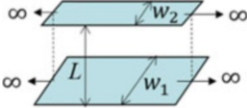
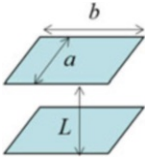
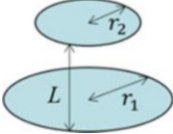
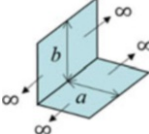
$$\alpha = \frac{\int_0^\infty \varepsilon_\lambda(\lambda) E_{b\lambda}(\lambda) d\lambda}{\int_0^\infty E_{b\lambda}(\lambda) d\lambda}, \quad (14.4)$$

In principle, $\alpha_\lambda(\lambda) = \varepsilon_\lambda(\lambda)$ for the same surface at a given wavelength [25]. However, the averaged values of those parameters are not necessarily equal to each other, i.e., $\alpha \neq \varepsilon$, because $G_\lambda(\lambda)$ coming from the sun at very high surface temperature ~ 5800 K is very different from $E_{b\lambda}(\lambda)$ coming from TE plate surface at much lower temperature below 1000 K. It is desirable for TE absorber to have high α for high $Q_{\text{rad, in}}$ and low ε for low heat loss by $Q_{\text{rad, out}}$.

In general case of radiant heat recovery system, heat source and TEG power system are placed within a certain distance, usually facing each other for high heat transfer between the two. Unlike the case in solar TE systems, $Q_{\text{rad, in}}$ is not constant but determined by the geometry of the system and optical/thermal characteristics of the objects involved. We model both the heat source and TE heat absorber as gray surfaces with emissivity ε_1 and ε_2 , respectively. Note that the emissivity is a function of temperature. For simplicity, emissivity is assumed to be constant in the operating temperature range in this chapter.

Unless one object is completely enclosed by the other, the surroundings will also participate in the radiation exchange as the third object. We assume the surroundings to be blackbody at ambient temperature T_{amb} . Then, one can determine the radiation

Table 14.1 Radiation shape factors for several common geometries [26]

Geometry	Shape factor F_{12}
Infinitely long concentric parallel plates 	$F_{12} = \sqrt{\left(\frac{L}{w_1}\right)^2 + \left(\frac{w_1 + w_2}{2w_1}\right)^2} - \sqrt{\left(\frac{L}{w_1}\right)^2 + \left(\frac{w_1 - w_2}{2w_1}\right)^2}$
Aligned parallel rectangles 	$A = a/L, B = b/L$ $F_{12} = \frac{2}{\pi AB} \left\{ \ln \sqrt{\frac{(1 + A^2)(1 + B^2)}{1 + A^2 + B^2}} + \right.$ $+ A\sqrt{1 + B^2} \left(\tan \frac{A}{\sqrt{1 + B^2}} \right)^{-1} + B\sqrt{1 + A^2} \left(\tan \frac{B}{\sqrt{1 + A^2}} \right)^{-1} -$ $\left. \frac{A}{\tan A} - \frac{B}{\tan B} \right\}$
Coaxial parallel disks 	$S_{dd} = 1 + \frac{L^2 + r_2^2}{r_1^2}$ $F_{12} = \frac{1}{2} \left\{ S_{dd} - \sqrt{S_{dd}^2 - 4 \left(\frac{r_2}{r_1} \right)^2} \right\}$
Infinitely long perpendicular plates with common edge 	$F_{12} = \frac{1 + \left(\frac{b}{a}\right) - \sqrt{1 + \left(\frac{b}{a}\right)^2}}{2}$

shape factor F_{ij} between each combination of two objects. Table 14.1 summarizes predetermined shape factors for several important geometries [26].

Once the shape factors are determined, radiation circuit can be constructed between three objects as shown in Fig. 14.3. Here, Objects 1, 2, and 3 in the circuit correspond to heat source, top of TE module and surroundings, respectively. Three nodes in the middle triangular circuit are associated with the radiosity J_i ($i = 1, 2, 3$) of each surface, and then each radiosity node is connected to each of the other two radiosity nodes with the appropriate space resistance R_{ij} determined by the corresponding shape factor and the surface area as displayed in Fig. 14.3. Each radiosity node is also connected to blackbody emissive power $E_{bi} = \sigma_{SB} T_i^4$ ($i = 1, 2, 3$) associated with temperature of that surface T_i using a surface resistance $R_{s,i}$. We used the relation $\rho_i = 1 - \epsilon_i$, where ρ_i is the reflectivity of i th surface with assumption of no transmission through the surface. Note that the

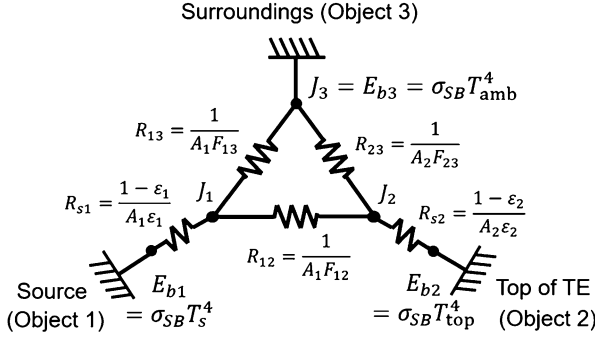


Fig. 14.3 Analogous circuit model for radiation transfer between heat source, TE module, and surroundings. Object 1 is the heat source with emissivity ϵ_1 . Object 2 is the top of TE module with emissivity ϵ_2 . Object 3 is the surroundings assumed black ($\epsilon_1 = 1$). R_{ij} refers to radiative resistance between two objects. F_{ij} is radiation shape factor from object i to j . E_{bi} is the emissive power at i th object, and J_i is the radiosity. A_1 and A_2 ($=A_{\text{total}}$) are the area of the heat source and TE module, respectively

radiosity of the surroundings is equal to its blackbody emissive power, i.e., $J_3 = E_{b3}$, as it is assumed to be black. So, there is no surface resistance for that node.

From the radiation network shown in Fig. 14.3, the net rate of heat transfer to TE surface can be found as a function of the emissive powers of three nodes by:

$$Q_{\text{rad,in}} - Q_{\text{rad,out}} = A_{\text{total}}(C_1 E_{b1} + C_2 E_{b2} + C_3 E_{b3}), \tag{14.5}$$

where coefficients C_i are found by applying Kirchoff’s circuit law to the radiation resistance network in Fig. 14.3 as:

$$C_1 = \frac{F_{12}\epsilon_1\epsilon_2}{a - F_{12}^2(1 - \epsilon_1)(1 - \epsilon_2)}, \tag{14.6}$$

$$C_2 = \frac{a\epsilon_2 [1 - F_{12}^2(1 - \epsilon_1)]}{a - F_{12}^2(1 - \epsilon_1)(1 - \epsilon_2)}, \tag{14.7}$$

$$C_3 = \frac{\epsilon_2 [a - F_{12}\epsilon_1 - F_{12}^2(1 - \epsilon_1)]}{a - F_{12}^2(1 - \epsilon_1)(1 - \epsilon_2)}, \tag{14.8}$$

where $a = A_2/A_1$ is area ratio of TE module area A_2 to source area A_1 . We assumed no self-radiation, i.e., $F_{ii} = 0$, and used the reciprocity theorem, i.e., $A_i F_{ij} = A_j F_{ji}$, to leave only one shape factor F_{12} , in the equations.

In addition, we model the convective heat loss at heat absorber surface with constant heat transfer coefficient h_{conv} as:

$$Q_{\text{conv,out}} = h_{\text{conv}} A_{\text{total}} (T_{\text{top}} - T_{\text{amb}}), \tag{14.9}$$

Finally, the total heat input entering TE elements is found using Eqs. (14.5) and (14.9) as:

$$Q_{\text{in,total}} = Q_{\text{rad,in}} - Q_{\text{rad,out}} - Q_{\text{conv,out}}, \quad (14.10)$$

14.2.2 Modeling of Individual TE Elements

For multielement TE module, we use two main design parameters as independent variables to optimize the performance. The first parameter is the fill factor F which is defined as the fractional area coverage of TE elements over the entire module area given by:

$$F = \frac{N_{\text{TE,pair}}(A_n + A_p)}{A_{\text{total}}}, \quad (14.11)$$

where $N_{\text{TE,pair}}$ is the number of n -type and p -type TE element pairs and A_n and A_p are cross-sectional area of individual n -type and p -type TE elements. Absorbed heat at the topside by the absorber is concentrated into smaller TE area by factor of $1/F$, which is greater than unity. This factor is called the *thermal concentration factor* [27]. In this work, we fix cross-sectional areas of individual elements and vary the spacing between TE elements to change fill factor. $N_{\text{TE,pair}}$ is changed accordingly for different fill factors by Eq. (14.11). The second design parameter is the thickness of TE elements L_{TE} . We use the same thickness for both n -type and p -type TE elements. By adjusting two parameters L_{TE} and F independently, both total thermal resistance and electrical resistance can be tuned independently and broadly to find out the optimal performances.

Our numerical model aims to solve simultaneously coupled thermal and electrical circuit equations for individual TE elements. The heat balance equations determine the temperature profile along TE element, whereas electrical circuit analysis with a load resistance determines electrical current, which again affects the heat balance equation. In order to obtain a detailed numerical analysis, temperature-dependent material properties are taken into account.

In order to obtain the accurate temperature profile and heat transfer rate in TE elements with temperature-dependent material properties taken into account, each TE element is divided into N segments with S_i , σ_i , and κ_i being Seebeck coefficient, electrical conductivity, and thermal conductivity, respectively, inside i th segment as shown in Fig. 14.4a. N must be sufficiently large, or the thickness of individual segments must be sufficiently small, so that temperature change within each segment can be assumed negligibly small. In this case, material properties S_i , σ_i , and κ_i in each segment can be assumed to be constant and obtained at average temperature of the segment, i.e., $(T_{i-1} + T_i)/2$.

Since the temperature in each segment is not known a priori, we make a guess for the initial temperature values at each node between segments and then assign the

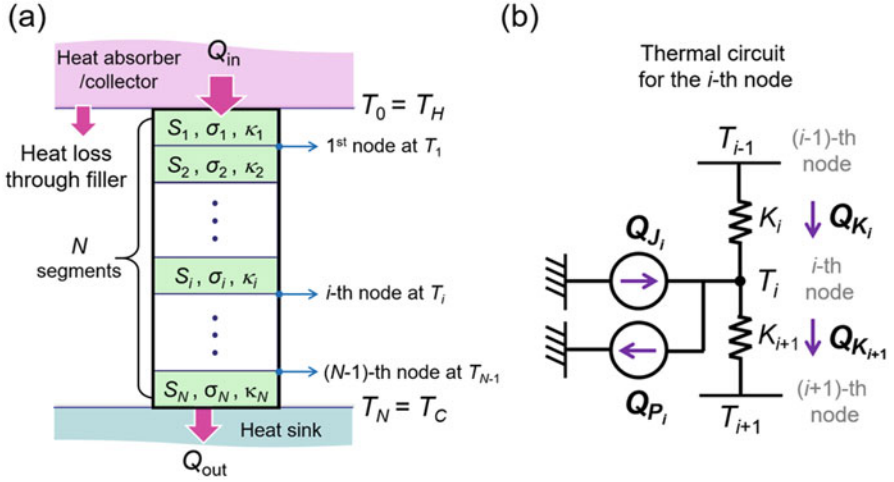


Fig. 14.4 (a) One-dimensional finite element model for single TE element divided into N segments for simulation with temperature-dependent material properties. (b) Thermal circuit at each node between segments, i.e., i th node, including three components of heat: conduction Q_{K_i} , Peltier/Thomson Q_{P_i} , and Joule terms Q_{J_i}

material properties in each segment corresponding to the temperature. By solving all the heat balance equations formulated at all the nodes simultaneously, we obtain updated temperature profile across TE element. Then a new set of material properties is allotted at each node based on updated temperatures for the next iteration. This process is repeated until the temperature profile converges within acceptable tolerance. A good initial guess for the temperature profile can be linear temperature distribution inside TE elements, assuming the conduction term is dominant over Joule and Peltier heat terms.

At one point of iteration, Q_{J_i} and Q_{P_i} at i th node and Q_{K_i} across i th segment are given by:

$$Q_{J_i} = \frac{1}{2}I^2R_i + \frac{1}{2}I^2R_{i+1}, \tag{14.12}$$

$$Q_{P_i} = (S_{i+1} - S_i)TiI, \tag{14.13}$$

$$Q_{K_i} = (T_{i-1} - T_i)K_i, \tag{14.14}$$

where I is electric current; $R_i = L_{TE}/(\sigma_i A_{TE} N)$ and $K_i = (\kappa_i A_{TE} N)/L_{TE}$ are, respectively, electrical resistance and thermal conductance of i th segment; and A_{TE} is cross-sectional area of individual TE elements, i.e., $A_{TE} = A_n$ for n -type and $A_{TE} = A_p$ for p -type elements. Figure 14.4b shows thermal resistance network model i th node. Hence, heat balance equation at i th node is:

$$Q_{J_i} - Q_{P_i} + Q_{K_i} - Q_{K_{i+1}} = 0, \tag{14.15}$$

where index i varies from 1 to $(N - 1)$ creating total of $(N - 1)$ equations to solve. It is noted that Peltier term between segments is non-zero if Seebeck coefficient varies with temperature. This is also called *Thomson effect* [28].

At 0th node or at the hot side of TE element, the heat balance equation has the same form as in Eq. (14.15) but with $i = 0$. At this node, Joule and Peltier terms have only one-side component because there is no Joule or Peltier effects from the top hot plate with no current flow. Also, Seebeck coefficient of electrode is assumed to be negligibly small. Thus:

$$Q_{J_0} = \frac{1}{2}I^2R_1, \quad (14.16)$$

$$Q_{P_0} = S_1T_0I, \quad (14.17)$$

where $T_0 = T_H$. The outgoing conduction term Q_{K_1} has the same form as in Eq. (14.14) but with $i = 1$, and the incoming conduction term Q_{K_0} from the top plate at 0th node is determined by heat transfer coefficient of the top plate ψ_h , and also the heat loss through the gap filler must be taken into account, such that, respectively:

$$Q_{K_1} = (T_0 - T_1)K_1, \quad (14.18)$$

$$Q_{K_0} = \frac{1}{F}A_{TE}\psi_h(T_{top} - T_0) - \frac{(1 - F)}{F} \frac{A_{TE}}{L_{TE}}\kappa_{filler}(T_0 - T_N), \quad (14.19)$$

where κ_{filler} is thermal conductivity of the gap filler in TE module, i.e., air. In Eq. (14.19), the first term on the right-hand side of the equation describes concentrated heat input to TE element by the concentration factor $1/F$. The second term is the heat lost through the filler by conduction, which is subtracted from the first term to get the net heat input into TE element.

Similarly, we can formulate the heat balance equation at N th node or at the cold side of individual TE elements using Eq. (14.15). Here, Joule and Peltier terms have only one-side component from N th segment of TE element because there is no Joule or Peltier effects from the bottom cold plate with no current flow. Thus:

$$Q_{J_N} = \frac{1}{2}I^2R_N, \quad (14.20)$$

$$Q_{P_N} = S_NT_NI, \quad (14.21)$$

where $T_N = T_C$. The incoming conduction term to N th node Q_{K_N} has the same form as in Eq. (14.14) but with $i = N$, and the outgoing conduction term $Q_{K_{N+1}}$ from N th node toward the cold plate is determined by the heat transfer coefficient of the cold plate ψ_c , such that, respectively:

$$Q_{K_N} = (T_{N-1} - T_N)K_N, \quad (14.22)$$

$$Q_{K_{N+1}} = A_{TE} \psi_c (T_N - T_{\text{bot}}) \times \frac{1}{F}, \quad (14.23)$$

where T_{bot} is assumed to be equal to the ambient temperature, i.e., $T_{\text{bot}} = T_{\text{amb}}$.

At the topside of module, another heat balance equation holds that the total incoming radiation heat transfer rate $Q_{\text{in,total}}$ obtained from Eq. (14.5) flows in the hot plate by conduction, such that:

$$Q_{\text{in,total}} = A_{\text{total}} \psi_h (T_{\text{top}} - T_h), \quad (14.24)$$

So far, we have constructed $N + 1$ heat balance equations given by Eq. (14.15) at $N + 1$ nodes with index i varying from 0 to N for TE element and another equation given by Eq. (14.24) for heat conduction through the hot plate, making the total number of equations $N + 2$. Since, there are the same number of unknown temperatures, i.e., T_i ($i = 0 \sim N$) and T_{top} , unique solution for temperature profile can be found that satisfies all the equations for a given electric current I . Electric current I will be determined by electric circuit model for the whole module with a load resistance connected, which will be discussed in the next subsection.

As discussed earlier, the found temperature values are reentered to update the material properties in each segment, and this process is iterated until the temperature profile converges.

14.2.3 Iterative Module Simulation

In the previous subsection, the heat balance equations for individual TE elements have been formulated. With these equations, temperature profiles for n -type and p -type elements are independently obtained. Since, n -type and p -type TE materials used have typically different material properties, hence temperature profiles will be different from each other. Thus, the topside temperature T_{top} on top of n -type TE element can be different from that of p -type one. This may not be physically reasonable because the hot plate is made of highly thermally conducting material for efficient heat transfer to TE elements, so temperature flattens quickly at the heat-absorbing surface. In reality, there will be lateral heat flow in the top plate between the regions of n -type and p -type elements to compensate nonuniformity in vertical heat flow between n -type and p -type elements [18]. To account for this effect in our one-dimensional finite element model, we add another heat exchange between two adjacent n -type and p -type TE elements in lateral direction inside the top plate, so that the heat input in each TE element is adjusted with that lateral heat exchange until the top temperature T_{top} becomes uniform.

Therefore, the heat input to n -type TE element previously given by Eq. (14.19) is corrected with additional lateral heat term to become:

$$Q_{\text{in},n} = Q_{K_0,n} = \frac{1}{F} A_n \psi_h (T_{\text{top}} - T_0) - \frac{1-F}{F} \frac{A_n}{L_n} \kappa_{\text{filler}} (T_0 - T_N) - Q_{\text{lateral}}, \quad (14.25)$$

By energy conservation, the same amount of heat must be added to the heat input to p -type TE element such that:

$$Q_{\text{in},p} = Q_{K_0,p} = \frac{1}{F} A_p \psi_h (T_{\text{top}} - T_0) - \frac{1-F}{F} \frac{A_p}{L_p} \kappa_{\text{filler}} (T_0 - T_N) + Q_{\text{lateral}}, \quad (14.26)$$

The lateral heat flow Q_{lateral} can be either positive or negative depending on direction of heat flows. Eqs. (14.25) and (14.26) are now used instead of Eq. (14.19) for simulation of n -type and p -type elements, respectively, to get final temperature profiles in those. Q_{lateral} must also be found by another iterative process to cause the topside temperature of n -type TE elements $T_{\text{top},n}$ and that of p -type ones $T_{\text{top},p}$ to converge with each other.

Lastly, electric current I flowing through TE module is determined from the analysis of electrical circuit with load resistance R_L . Since, all the elements, electrodes, and load resistances are connected electrically in series, adding all resistances from those along with contact resistances results in the total internal electrical resistance in TE module given by:

$$R_{\text{int}} = \sum \left(\sum_i R_i + 2R_c + 2R_{\text{el}} \right), \quad (14.27)$$

where $\sum_i R_i$ is internal resistance of each TE element obtained by adding the resistances from all the segments of TE element. R_c is contact resistance per one side of TE element, and R_{el} is electrode resistance per one side of TE element. Symbol Σ indicates the summation over all TE elements. In TE module, open-circuit voltage V_{OC} is created by Seebeck effects inside TE elements. In each segment of TE element, Seebeck voltage is obtained as:

$$V_{\text{OC}_i} = S_i (T_i - T_{i-1}), \quad (14.28)$$

Then, total V_{OC} is obtained by adding all Seebeck voltages over all segments of all TE elements, thus by two-stage summation as:

$$V_{\text{OC}} = \sum \sum_i V_{\text{OC}_i}, \quad (14.29)$$

Finally, electric current I is obtained by Ohm's law for electric circuit model as:

$$I = \frac{V_{\text{OC}}}{R_{\text{int}} + R_L}, \quad (14.30)$$

In short, the total number of unknown variables that need to be solved simultaneously for simulation of TE element becomes $N + 3$, i.e., T_i ($i = 0$ to N), T_{top} , and I . These unknown variables can be determined by solving simultaneously of $N + 3$ equations (15) for ($i = 0 \sim N$) and (24) and (30). After solving $N + 3$ multiple equations together, obtained temperature profile is plugged back in the same equations to update the material properties and then solved again iteratively until the temperature profile converges. Iterative process is performed independently for each n -type and p -type TE element, and then the second-level iteration is performed to make $T_{top,n}$ and $T_{top,p}$ converge as discussed above to complete TE module simulation. The flow chart for two-level iterative module simulation is displayed in Fig. 14.5.

Finally, TE module performances are calculated from obtained temperature profiles, total heat flow, and electric current. The voltage output, power output,

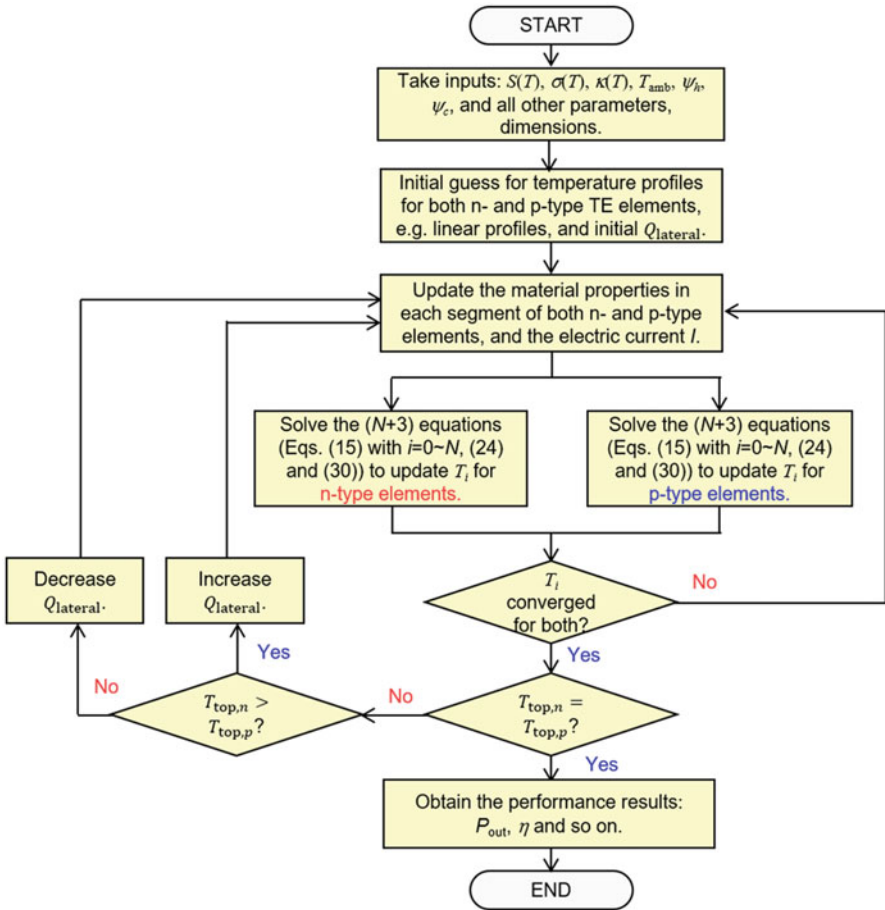


Fig. 14.5 Flow chart of two-level iteration algorithm to solve for temperature profiles and heat transfer in n -type and p -type TE elements and the performance of the entire TE module

total heat input to TE, TE efficiency, and the system efficiency are obtained, respectively, by:

$$V_{\text{out}} = IR_L, \quad (14.31)$$

$$P_{\text{out}} = IV_{\text{out}}, \quad (14.32)$$

$$Q_{\text{in,TE}} = N_{\text{TE,pair}}(Q_{\text{in,n}} + Q_{\text{in,p}}), \quad (14.33)$$

$$\eta_{\text{TE}} = \frac{P_{\text{out}}}{Q_{\text{in,TE}}}, \quad (14.34)$$

$$\eta = \frac{P_{\text{out}}}{Q_{\text{in,system}}}, \quad (14.35)$$

where $Q_{\text{in,system}}$ is the total heat input transferred from the source to the system before heat losses occur, i.e., $Q_{\text{in,system}} = GCA_{\text{total}}$ for solar TE system and $Q_{\text{in,system}} = \varepsilon_1 F_{12} \sigma_{\text{SB}} T_{\text{source}}^4 A_1$ for general radiant heat recovery system with the heat source at T_{source} . The system efficiency η takes into account all optical, radiative, and convection heat losses, so that it is always lower than TE efficiency. The load resistance R_L is independent parameter, but for maximum power delivery, it can be set to be equal to the internal resistance, i.e., $R_L = R_{\text{int}}$, which is known as the *electrical load matching* condition [14.28].

14.3 Solar Thermoelectric Generation

In this section, we present detailed simulation results obtained using simulation methods described in the previous section for solar thermoelectric systems. As shown in Fig. 14.1a earlier, our solar TE system consists of multielement TE module, solar absorber attached to the topside of the module, heat sink for efficient heat removal at the bottom side, and solar concentrator, e.g., Fresnel lens, for high-density heat input. We don't assume vacuum enclosure for the system as it can add substantial installation and maintenance costs. Convection heat loss is thus included in the simulation. We will compare the performances in vacuum and in air. Also, we use the same area of absorber as that of TE module without significant thermal concentration by the area shrinkage in effort to minimize the nonuniform temperature distribution over the absorber area. Yet, fill factor less than unity will cause similar effects of thermal concentration in TE module. Multielement module is used to produce not only high efficiency or power output but also high-voltage output required for powering electronics above 1–3 V as the voltage increases in proportion to the number of TE elements. Air gap is used as the filler between TE elements. The

fill factor and thickness of TE elements are varied to optimize the performance. Table 14.2 summarizes the system design parameters used in the simulation.

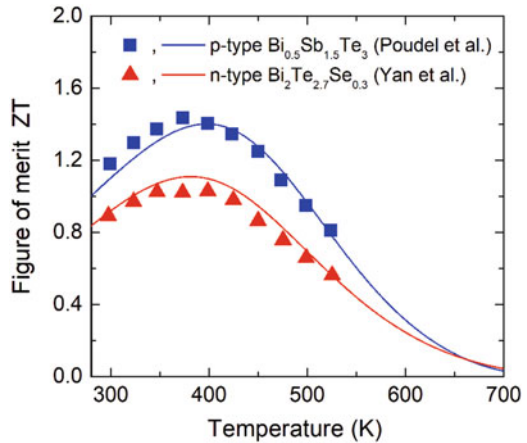
We use the state-of-the-art nanostructured bismuth telluride alloy materials, $\text{Bi}_2\text{Te}_{2.7}\text{Se}_{0.3}$ for n -type and $\text{Bi}_{0.5}\text{Sb}_{1.5}\text{Te}_3$ for p -type TE elements in this study. Figure 14.6 shows the figure-of-merit ZT of TE materials as a function of temperature. The complete material properties are given in [29] and [30], respectively. These materials have peak value $ZT = 1.4$ for p -type and $ZT \sim 1.0$ for n -type, both at around 400 K. Beyond peak temperature, ZT value decreases significantly with increasing in temperature. For temperature ranges where the experimental material properties are not available, we calculated the material properties based on linearized Boltzmann transport model based on fitting of the experimental data. Details about the material modeling are given in [32].

Values of absorptivity ($\alpha = 0.9$) and emissivity ($\epsilon = 0.15$) used for solar absorber are adapted from [16], which is experimentally determined for black-painted

Table 14.2 System parameters used in the numerical analysis for solar TE systems

Material for n -type TE elements	Nanostructured $\text{Bi}_2\text{Te}_{2.7}\text{Se}_{0.3}$ [29]
Material for p -type TE elements	Nanostructured $\text{Bi}_{0.5}\text{Sb}_{1.5}\text{Te}_3$ [30]
Solar irradiation, G	700 W/m^2
Mean transmissivity of solar concentrator, τ	0.94 [13]
Mean absorptivity of solar absorber, α	0.9 [16]
Mean emissivity of solar absorber, ϵ	0.15 [16]
Temperature of TE bottom, $T_{\text{bot}} (= T_{\text{amb}})$	300 K
Cross-sectional area of TE elements, $A_n = A_p$	$2 \times 2 \text{ mm}^2$
Total area of TE module, A_{total}	$10 \times 10 \text{ cm}^2$
Heat transfer coefficient of hot-side plate, ψ_h	$5000 \text{ W} \times \text{m}^{-2} \times \text{K}^{-1}$
Heat transfer coefficient of cold-side heat sink, ψ_c	$3000 \text{ W} \times \text{m}^{-2} \times \text{K}^{-1}$ [31]
Convection heat transfer coefficient at hot side, h_{conv}	$20 \text{ W} \times \text{m}^{-2} \times \text{K}^{-1}$
Thermal conductivity of filler (air), κ_{filler}	$0.04 \text{ W} \times \text{m}^{-1} \times \text{K}^{-1}$

Fig. 14.6 Figure-of-merit ZT as a function of temperature for both n -type [29] and p -type [30] TE materials used in solar TE system simulation. Symbols are experimental data, and lines are theoretical fitting [32]



spectrally selective solar absorber. Detailed information about solar absorber is found in [33]. As discussed earlier in Sect. 14.2.1, these two values are very different from each other because the absorptivity is a mean value given by Eq. (14.2) for the solar irradiation at ~ 5800 K, while the emissivity is a mean value given by Eq. (14.4) at the absorber temperature around 600–900 K, which is mostly in infrared region.

The hot-side heat transfer coefficient ψ_h is assumed to be $5000 \text{ Wm}^{-2} \text{ K}^{-1}$, assuming highly conductive plate with sufficiently small thickness. At the cold side, high-efficiency water-cooling heat sink is assumed in order to remove such high heat flux. A micro-channel heat sink can achieve net heat transfer coefficient ψ_c as high as $4000 \text{ W} \times \text{m}^{-2} \times \text{K}^{-1}$ or even higher [31]. We choose conservatively value of $3000 \text{ W} \times \text{m}^{-2} \times \text{K}^{-1}$ for ψ_c and later vary two external heat transfer coefficient values to quantify impacts on P_{out} .

14.3.1 Module Optimization

Figure 14.7 shows the module simulation results for $10 \times 10 \text{ cm}^2$ area solar TE module under solar concentration of 60 suns. We varied the thickness of TE elements and the fill factor to optimize the performance. Figure 14.7a shows that hot-side temperature T_H increases and cold-side temperature T_C decreases as the thickness of TE elements increases because thermal resistance of TE elements increases with the thickness, which causes temperature difference applied to TE elements to rise up. Due to the increase in the total thermal resistance in heat flow direction, $Q_{\text{in, TE}}$ drops gradually with increasing thickness as shown in Fig. 14.7b. On P_{out} , however, the impact of TE element thickness is mixed. In the beginning, P_{out} increases with increasing in thickness due to increased temperature difference, which causes V_{out} to increase. But, at the same time, $Q_{\text{in, TE}}$ decreases due to increased thermal resistance, and, also, I decreases due to increased electrical resistance with increasing thickness. Hence, P_{out} decreases later in high-thickness region. Due to this trade-off, there is optimal thickness that maximizes P_{out} as shown in Fig. 14.7c. The optimal thickness is shifted to larger value as the fill factor F increases because increase in fill factor can neutralize the negative impact of increasing in thickness on $Q_{\text{in, TE}}$. As shown in Fig. 14.7b, $Q_{\text{in, TE}}$ increases with increasing in fill factor at fixed thickness because increased fill factor reduces the thermal resistance of TE module. Thus, larger thickness is required to maintain the optimal P_{out} for larger fill factor design. Both larger thickness and larger fill factor mean increase in the volume of material used and thus increase in the material cost, which is detrimental.

On the other hand, small thickness with small F can maintain the peak P_{out} high while keeping the material cost lower, thereby reducing the material cost per power. It is important to note that if either thickness or F is too low, the peak P_{out} can be substantially reduced as shown in Fig. 14.7c because the heat input gets too low and, also, the positive effect of increased temperature difference is mitigated by the decreased material figure-of-merit. As discussed above, material ZT drops

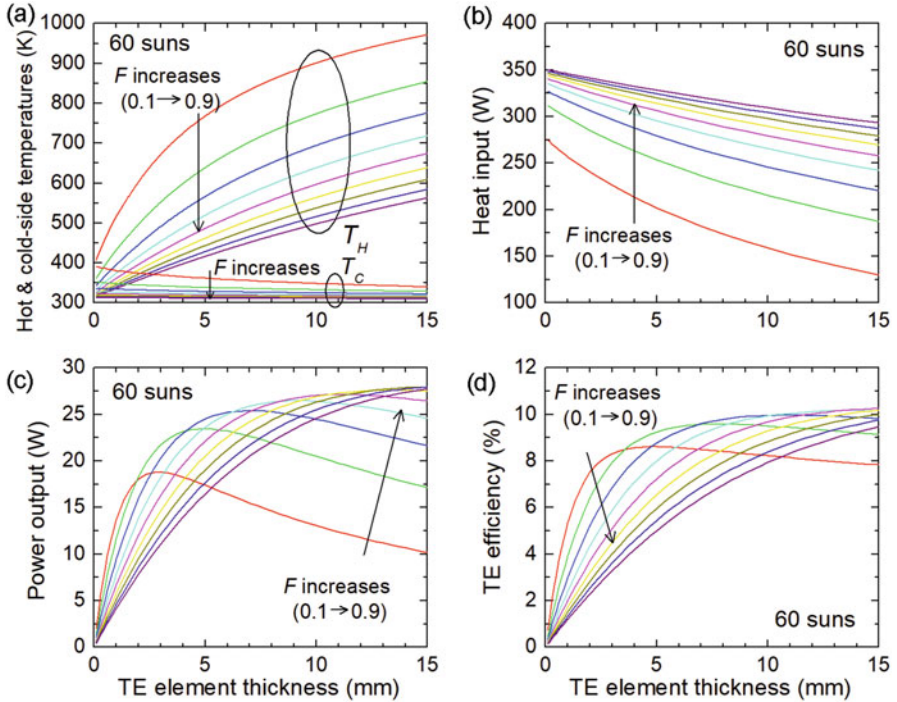
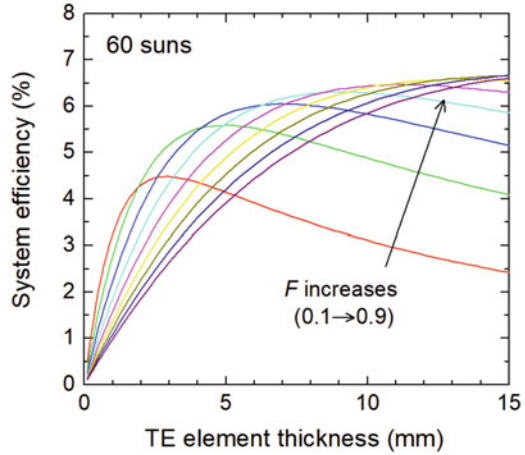


Fig. 14.7 (a) Hot-side T_H and cold-side T_C temperatures of TE elements $Q_{in, TE}$; (b) total heat input to TE elements $Q_{in, TE}$; (c) power output P_{out} ; and (d) TE efficiency η_{TE} of $10 \times 10 \text{ cm}^2$ solar TE module under solar concentration $C = 60$ suns as a function of TE element thickness with varying fill factor F from 0.1 to 0.9 with step size of 0.1

significantly with temperature above 400 K due to bipolar transport effect. Since hot-side temperature increases beyond 600 K, where material ZT is less than 0.2, the increased temperature difference would not help increase much V_{out} and P_{out} for F lower than 0.2. Reduced η_{TE} for low F confirms this argument (Fig. 14.7d). η_{TE} should have increased with increasing in temperature difference at lower F if average ZT was maintained the same. But, average ZT was reduced due to too high hot-side temperature, which resulted in lower η_{TE} as shown in Fig. 14.7d. Therefore, we may keep F at ~ 0.2 (green line in Fig. 14.7) and use the thickness slightly less than optimal (< 4 mm) to keep P_{out} and η_{TE} high and the material cost-per-power low.

Figure 14.8 shows calculated system efficiency η of the same system. Compared to corresponding η_{TE} shown in Fig. 14.7d, η is much lower due to heat losses at the concentrator and the absorber and through the filler. As F decreases, the reduction in maximum efficiency becomes even more significant, because hot-side temperature increases with decreasing F , which in turn increases in heat losses by back-radiation and convection at the top surface; η above 5% is still possible with F of 0.2 and thickness of 3 mm. Higher $\eta \sim 6.5\%$ is possible if F is larger than 0.5 and thickness greater than 8 mm.

Fig. 14.8 System efficiency η of $10 \times 10 \text{ cm}^2$ solar TE module under solar concentration $C = 60$ suns as a function of TE element thickness with varying fill factor F from 0.1 to 0.9 with step size of 0.1



14.3.2 Performance Variation with Solar Concentration in Air/Vacuum

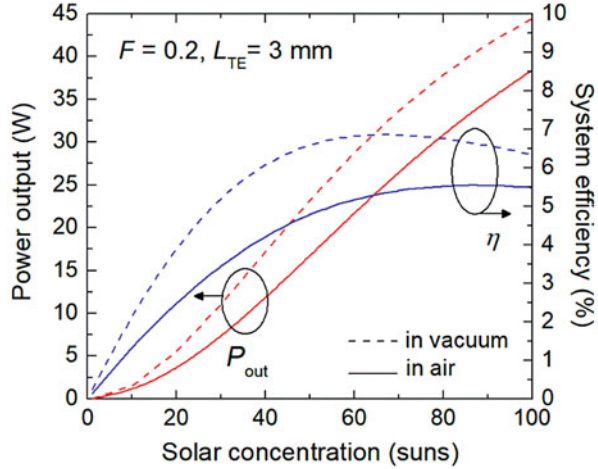
In the discussion above, we fixed the solar concentration at 60 suns. But the system performance can be further tuned with varying solar concentration. Figure 14.9 shows the simulation results of P_{out} and η of $10 \times 10 \text{ cm}^2$ area solar TE module with varying solar concentration. Here we fixed F at 0.2 and TE element thickness at 3 mm for optimal performance.

As shown in Fig. 14.9, both P_{out} and η rapidly increase with increasing in solar concentration initially. This is due to increased $Q_{\text{in, TE}}$ and increased temperature difference across TE. However, if solar concentration increases too high, hot-side temperature increases substantially, which increases in heat loss from the top surface, thereby limiting η and η saturates at $\sim 5.5\%$ above 70 suns in the case of usual operation in air without vacuum enclosure. In vacuum, the convection heat loss is removed, so that higher η can be achieved. However, the temperature increases even further in vacuum, which increases in radiation heat loss at the top surface. Increased temperature would also limit the increasing in rate of P_{out} with concentration, because average ZT of TE materials in the module will be decreased in high-temperature range. Therefore, η even slightly decreases beyond 70 suns. Thus, peak $\eta \sim 7\%$ is achieved under moderate solar concentration of ~ 60 suns. P_{out} is about 30% larger in vacuum than that in air over the entire solar concentration range.

14.3.3 Impact of External Heat Transfer Coefficients

In system performance, external heat transfer coefficients at hot and cold sides of TE module (ψ_{h} and ψ_{c} , respectively) are also very important factors. It is known that

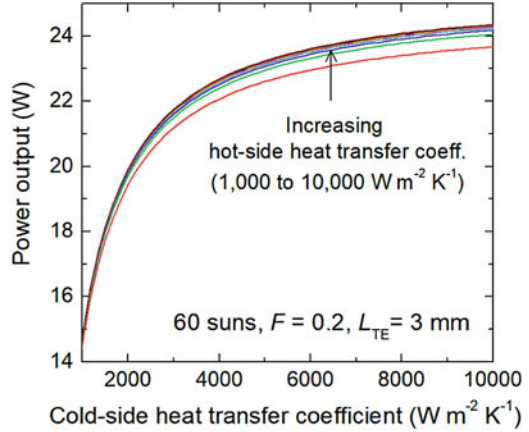
Fig. 14.9 Power output P_{out} (left y-axis) and system efficiency η (right y-axis) as a function of solar concentration for $10 \times 10 \text{ cm}^2$ solar TE module with $F = 0.2$ and TE element thickness $L_{\text{TE}} = 3 \text{ mm}$. Solid curves are properties of the system in air, and dash curves are those in vacuum



maximum P_{out} can be achieved when total external thermal resistance, i.e., $1/(\psi_h A_{\text{total}}) + 1/(\psi_c A_{\text{total}})$, is equal to total thermal resistance from TE elements assuming that Peltier and Joule heat are much smaller than conduction heat in TE module. This is called the *thermal matching* condition. However, this condition is derived under temperature boundary conditions. In radiant heat recovery applications, however, temperatures at the boundaries are not constant, but rather change a lot with many different system parameters. So, P_{out} may change in more complicated ways with the heat transfer coefficients. Nonetheless, since we are aiming at using thin TE elements to minimize cost-per-power, external thermal resistances need to be sufficiently high.

We have simulated TE module performance with varying both ψ_h and ψ_c and calculated P_{out} is shown as a function of those parameters in Fig. 14.10. Here we used $F = 0.2$ and element thickness of 3 mm under 60 suns. First, P_{out} increases with increasing in ψ_c and becomes almost flattened at high-coefficient region above $\sim 4000 \text{ W} \times \text{m}^{-2} \times \text{K}^{-1}$. In fact, it is very difficult to achieve high ψ_c beyond this value with active water-cooling heat sink. However, if ψ_c is less than $3000 \text{ W} \times \text{m}^{-2} \times \text{K}^{-1}$, P_{out} is severely suppressed due to the inability in efficient heat removal at the cold side, which increases cold-side temperature of TE elements and limits the temperature difference. Particularly for the materials used in TE module, those high ZT values lie in low temperature range below 500 K. Therefore, it is critical to let those temperature ranges be applied across TE elements with strong heat sink. On the other hand, the effect of ψ_h is not as significant as shown in Fig. 14.10. Since hot-side temperature is already high enough due to high solar concentration and low F , an increase in ψ_h does not help further enhance P_{out} because material ZT is too low at added temperature range induced by increased ψ_h . For example, an increase of ψ_h from 1000 to 10,000 $\text{W} \times \text{m}^{-2} \times \text{K}^{-1}$ can improve P_{out} merely by 5% or less, according to Fig. 14.10.

Fig. 14.10 Power output P_{out} as a function of cold-side heat transfer coefficient ψ_c with varying hot-side heat transfer coefficient ψ_h for $10 \times 10 \text{ cm}^2$ solar TE module with $F = 0.2$ and TE element thickness $L_{\text{TE}} = 3 \text{ mm}$ under 60 suns in air



14.4 Radiant Heat Recovery in Hot Steel Casting

In this application, we consider hot steel casting belt carrying steel slabs at temperatures as high as 1200 K or above as schematically shown earlier in Fig. 14.1b. When TE modules are installed above the casting belts, facing down to the slabs in parallel, strong radiation is transferred to TE module. We assume steel slabs continuously sliding along the belts and TE system of the same width as the slabs directly above the slabs. This configuration can be modeled as two infinitely long concentric parallel plates shown as the first geometry in Table 14.1 but with the same width, i.e., $w_1 = w_2$. Thus, the radiation shape factor from the slab to TE system is found from Table 14.1 as:

$$F_{12} = \left(\sqrt{\left(\frac{L_{\text{slab}}}{w_{\text{slab}}} \right)^2 + 1} \right) - \frac{L_{\text{slab}}}{w_{\text{slab}}}, \quad (14.36)$$

where L_{slab} is vertical distance between steel slab and TE module and w_{slab} is width of the slab and TE absorber plate.

Just like in solar TE systems discussed in the previous section, we use multielement TE modules with heat absorber plate at hot side, facing down toward hot steel slabs, and heat sink at cold side for efficient heat removal to ambient. Note that the following simulation results are calculated for $10 \times 10 \text{ cm}^2$ size of TE module. Since width and length of entire TE system are much larger than individual TE module size, multiple modules are installed to cover the entire area. Here, we assume that all TE modules share large heat-absorbing plate at hot side and heat absorber plate is so highly conducting that it can uniformly distribute the heat input to each of the TE modules. Hence, total P_{out} is simply P_{out} of one module multiplied by the number of modules used to cover the entire area. In this case, the total heat input from the slab to each module of area A_{total} is given by:

Table 14.3 System parameters used in simulation for radiant heat recovery system in hot steel casting

Material for n -type TE elements	Nanostructured $\text{Bi}_2\text{Te}_{2.7}\text{Se}_{0.3}$ [29]
Material for p -type TE elements	Nanostructured $\text{Bi}_{0.5}\text{Sb}_{1.5}\text{Te}_3$ [30]
Slab temperature, T_{slab}	1200 K [17]
Slab width, w_{slab}	2 m [17]
Distance between slab and TE system, L_{slab}	2 m
Mean emissivity of hot steel slab, ε_1	0.7 [34]
Mean emissivity of heat absorber, ε_2	0.9 [33]
Mean absorptivity of heat absorber, $\alpha_2(=\varepsilon_2)$	0.9 [33]
Temperature of TE bottom, $T_{\text{bot}}(=T_{\text{amb}})$	300 K
Cross-sectional area of TE elements, $A_n = A_p$	$2 \times 2 \text{ mm}^2$
Total area of TE module, A_{total}	$10 \times 10 \text{ cm}^2$
Heat transfer coefficient of hot-side plate, ψ_h	$5000 \text{ W} \times \text{m}^{-2} \times \text{K}^{-1}$
Heat transfer coefficient of cold-side heat sink, ψ_c	$3000 \text{ W} \times \text{m}^{-2} \times \text{K}^{-1}$ [31]
Convection heat transfer coefficient at hot side, h_{conv}	$20 \text{ W} \times \text{m}^{-2} \times \text{K}^{-1}$
Thermal conductivity of filler (air), κ_{filler}	$0.04 \text{ W} \times \text{m}^{-1} \times \text{K}^{-1}$

$$Q_{\text{in,system}} = \varepsilon_1 F_{12} \sigma_{\text{SB}} T_{\text{slab}}^4 A_{\text{total}}, \quad (14.37)$$

where ε_1 and T_{slab} are, respectively, emissivity and temperature of the slab surface. Note that the shape factor F_{12} here was obtained for two parallel plates of the same width, i.e., $A_1 = A_2$. To get the total heat input transferred to smaller module area A_{total} only, area ratio A_{total}/A_2 was multiplied to source area A_1 to simply reduce to A_{total} at the end of Eq. (14.37). This $Q_{\text{in, system}}$ is used in Eq. (14.35) to calculate η .

We use the same TE materials used in solar TE for this application. The steel emissivity is as low as 0.2–0.3 below 400 °C, but it increases to 0.7 above 500 °C [34]. We use 0.7 as the emissivity of steel slab that is at 1200 K. We use the same absorber used in solar TE system simulation in the previous section. The absorptivity of absorber is 0.9 in infrared region. The emissivity of absorber must be almost the same (0.9) as its absorptivity because the absorber also emits in infrared region. Other parameters are also assumed to be the same as in the case of solar TE system. Table 14.3 summarizes the system parameters used in this hot steel casting application.

14.4.1 Module Optimization

Figure 14.11 presents calculated module performances with varying TE element thickness and F for $10 \times 10 \text{ cm}^2$ TE module size. As was similarly shown in solar TE system in the previous section, by adjusting thickness and F , one can broadly tune heat input and P_{out} to meet the design goals. There is optimal thickness that maximizes P_{out} for a given F . For example, for $F = 0.2$ (green curves in Fig. 14.11),

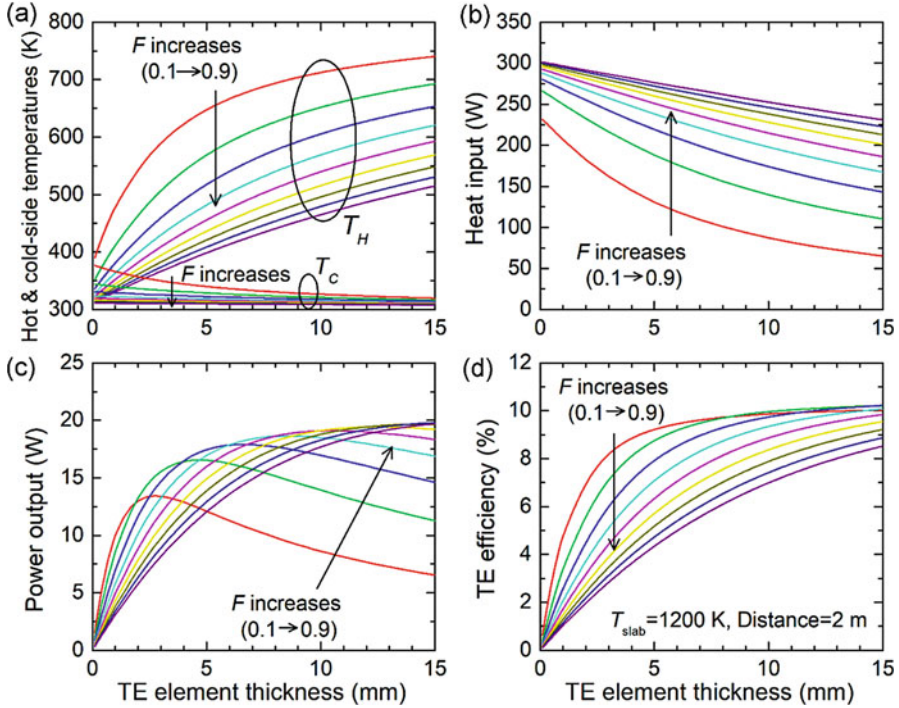


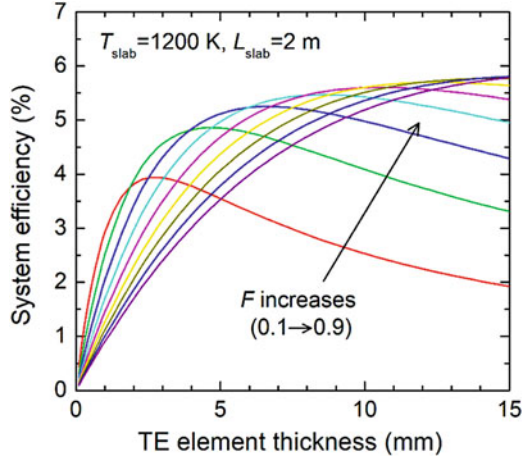
Fig. 14.11 (a) Hot-side T_H and cold-side T_C temperatures of TE elements $Q_{\text{in,TE}}$; (b) total heat input to TE elements $Q_{\text{in,TE}}$; (c) power output P_{out} ; and (d) TE efficiency η_{TE} of $10 \times 10 \text{ cm}^2$ TE module for radiant heat recovery in hot steel casting application. All the properties are displayed as a function of TE element thickness with varying fill factor F from 0.1 to 0.9 with step size of 0.1. The temperature of hot steel slab is 1200 K, and distance between TE module and the slab is 2 m

P_{out} is maximized to reach ~ 16.5 Watt at TE element thickness ~ 5 mm. However, P_{out} is quite flat over certain range of thickness near this optimal thickness. This means that by choosing smaller thickness near the optimal value, P_{out} very close to the maximum can be still achieved, while the material cost can be lowered. For example, one can select thickness of 3 mm instead of 5 mm, for which P_{out} is as high as 15.5 Watt, only $\sim 5\%$ lower than the maximum P_{out} .

As F decreases, the temperature difference between hot side and cold side of TE module increases as shown in Fig. 14.11a, which increases in η_{TE} (Fig. 14.11d), except for high-thickness region for $F = 0.1$. In this region, low $F = 0.1$ caused hot-side temperature to be too high, which resulted in lowering average ZT , so that η_{TE} was reduced from that of $F = 0.2$.

The heat input is reduced (Fig. 14.11b) as F decreases, because of increased module thermal resistance. So, P_{out} is reduced accordingly even though η_{TE} was slightly higher. Moreover, heat loss by radiation is increased as hot-side temperature increases, which results in lower η as shown in Fig. 14.12.

Fig. 14.12 System efficiency η as a function of TE element thickness for $10 \times 10 \text{ cm}^2$ TE module for radiant heat recovery in hot steel casting application. F varied from 0.1 to 0.9 with step size of 0.1. Slab temperature is 1200 K, and distance between TE module and slab is 2 m



As discussed similarly in solar TE systems, we could estimate power-per-cost might be achieved for hot steel casting application.

14.4.2 Performance Variation with Distance Between TE Module and Slab

If distance between TE module and slab is reduced, by placing TE system closer toward the slab, then radiation shape factor increases according to Eq. (14.36), which results in more heat transfer to TE system. As shown in Fig. 14.13a, both heat input and hot-side temperature increase with decreasing distance between TE module and slab. This results in increase in P_{out} (Fig. 14.13b). High P_{out} larger than 25 Watts can be generated for slab distance shorter than 1 m according to the calculation.

Value η also improves with decreasing distance between TE module and slab initially from 4 m until ~ 1 m and then saturates below 1 m distance. This is due to increased hot-side temperature (Fig. 14.13a) causing more heat losses and thus reducing η . The reduced material figure-of-merit also plays a role in reducing η in this regime. Maximum $\eta \sim 5.3\%$ is obtained here with distance between TE module and the slab from 0.5 m to 1 m.

14.4.3 Performance Variation with Slab Temperature

One can improve P_{out} by increasing in slab temperature too because more radiant heat is transferred to TE system. As shown in Fig. 14.14, P_{out} rapidly increases with slab temperature, almost following $\sim T^4$. At high slab temperature region, η is again saturated at its maximum $\sim 5.3\%$ due to increased heat losses, which in turn lessens

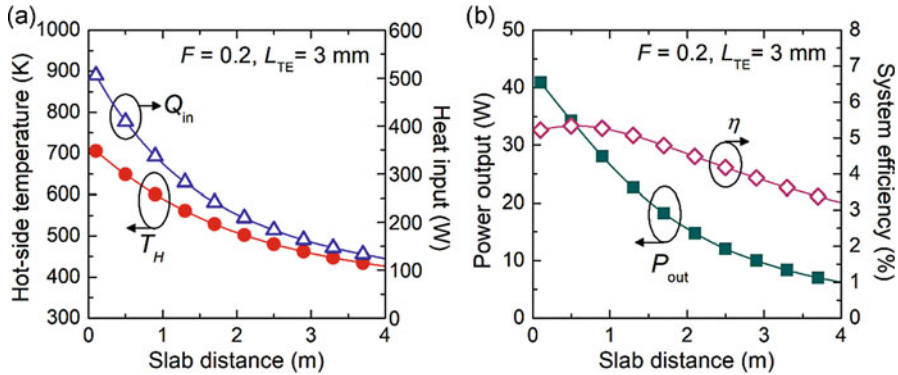
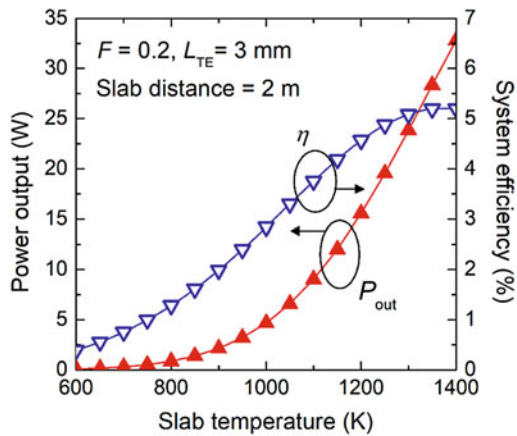


Fig. 14.13 (a) Hot-side temperature T_H (left y- axis) and heat input $Q_{in, TE}$ (right y- axis) and (b) power output P_{out} (left y- axis) and system efficiency η (right y- axis) as a function of distance between TE module and slab for $10 \times 10 \text{ cm}^2$ TE module for radiant heat recovery in hot steel casting application. Slab temperature is fixed at 1200 K. $F = 0.2$ and TE element thickness $L_{TE} = 3 \text{ mm}$ were used for TE module

Fig. 14.14 Power output P_{out} (left y-axis) and system efficiency η (right y- axis) as a function of slab temperature for $10 \times 10 \text{ cm}^2$ TE module for radiant heat recovery in hot steel casting. $F = 0.2$ and TE element thickness $L_{TE} = 3 \text{ mm}$ were used. Distance between TE module and slab was fixed at 2 m



increasing in rate of P_{out} with slab temperature in high-temperature region. At low slab temperature region below 800 K, P_{out} is merely 1 Watt or less for $10 \times 10 \text{ cm}^2$ TE module, which is much lower than $P_{out} \sim 15$ Watt when slab temperature of 1200 K; η is also lower than 1%, accordingly. This result may imply that TE-based radiant heat recovery may not be efficient solution if temperature of heat source is less than 800–1000 K. Contact-based TE conversion may be considered instead for more efficient energy conversion. Yet, the performance of TE-based radiant heat recovery system can be improved by increasing in shape factor, e.g., placing TE module closer, enclosing the source with TE, and so on, and by improving TE materials, heat absorber, and heat sink.

14.5 Conclusions

In this chapter, we have presented our TE module simulation methodology and theory based on two-level iterative finite element analysis for radiant heat recovery applications. Detailed performance analysis and design optimization have been discussed for two major applications, solar and radiant heat recovery in hot steel casting processes. In both applications, careful analysis on the radiant heat inputs and various heat losses based on optical parameters and geometry of the system was the key to accurate prediction of energy conversion performance. By optimizing TE element thickness and fill factor, thermal and electrical properties of TE module can be broadly tuned to achieve maximum power output, system efficiency, or power-per-cost to make TE radiant heat recovery technology potentially competitive with other leading energy conversion technologies at the market level.

The system efficiency can be further enhanced by improving the heat transfer media such as heat absorber and heat sink used and, also, by improving TE materials' performance. The low performance of nanostructured bismuth telluride alloy materials used in our simulation at high temperatures above 600 K has limited TE efficiency to maximum $\sim 10\%$ in both systems, which in turn limited the system efficiency. Segmented TE elements would be helpful to increase TE efficiency as recently demonstrated [16].

Acknowledgment J.H. Bahk is grateful for the generous faculty start-up supports for this work from the University of Cincinnati.

References

1. L.E. Bell, Cooling, heating, generating power, and recovering waste heat with thermoelectric systems. *Science* **321**, 1457 (2008)
2. D. Champier, Thermoelectric generators: a review of applications. *Energy Convers. Manag.* **140**, 167–181 (2017)
3. W. Corliss, D. Harvey, *Radioisotopic Power Generation* (Prentice-Hall, Englewood Cliffs, NJ, 1964)
4. J.C. Bass, N. Elsner, F. Leavitt, Performance of the 1 kW thermoelectric generator for diesel engines, in *Proceedings of the XIII International Conference on Thermoelectrics* (Kansas City, MO, 1994)
5. M. Zebarjadi, Electronic cooling using thermoelectric devices. *Appl. Phys. Lett.* **106**, 203506 (2015)
6. R. Vullers, R.v. Schaijk, H.J. Visser, J. Penders, C.V. Hoof, Energy harvesting for autonomous wireless sensor networks. *IEEE Solid State Circ. Mag.* **2**(2), 29–38 (2010)
7. R. Funahashi, M. Mikami, T. Mihara, S. Urata, N. Ando, A portable thermoelectric-power-generating module composed of oxide devices. *J. Appl. Phys.* **99**, 066117 (2006)
8. J.-H. Bahk, H. Fang, K. Yazawa, A. Shakouri, Flexible thermoelectric materials and device optimization for wearable energy harvesting. *J. Mater. Chem. C* **3**, 10362–10374 (2015)
9. Y. Shuai, X.-L. Xia, H.-P. Tan, Radiation performance of dish solar concentrator/cavity receiver systems. *Sol. Energy* **82**(1), 13–21 (2008)
10. W. Xie, Y. Dai, R. Wang, K. Sumathy, Concentrated solar energy applications using fresnel lenses: a review. *Renew. Sust. Energ. Rev.* **15**, 2588–2606 (2011)

11. A. Al-Merbaty, B. Yilbas, A. Sahin, Thermodynamics and thermal stress analysis of thermoelectric power generator: influence of pin geometry on device performance. *Appl. Therm. Eng.* **50**(1), 683–692 (2013)
12. D. Narducci, P. Bermel, B. Lorenzi, N. Wang, K. Yazawa, *Hybrid and Fully Thermoelectric Solar Harvesting* (Springer, New York, 2018)
13. M. Telkes, Solar thermoelectric generators. *J. Appl. Phys.* **25**, 765 (1954)
14. D. Kraemer, B. Poudel, H.-P. Feng, J.C. Caylor, B. Yu, X. Yan, Y. Ma, X. Wang, D. Wang, A. Muto, K. McEnaney, M. Chiesa, Z. Ren, G. Chen, High-performance flat-panel solar thermoelectric generators with high thermal concentration. *Nat. Mater.* **10**, 532–538 (2011)
15. D. Kraemer, K. McEnaney, Z. Ren, G. Chen, Concept of solar thermoelectric power conversion, in *Thermoelectrics and its Energy Harvesting*, (CRC Press, New York, 2012), p. 24.1
16. D. Kraemer, Q. Jie, K. McEnaney, F. Cao, W. Liu, L.A. Weinstein, Concentrating solar thermoelectric generators with a peak efficiency of 7.4%. *Nat. Energy* **1**, 16153 (2016)
17. T. Kuroki, K. Kabeya, K. Makino, T. Kajihara, H. Kaibe, H. Hachiuma, H. Matsuno, A. Fujibayashi, Thermoelectric generation using waste heat in steel works. *J. Electron. Mater.* **43**(6), 2405–2410 (2014)
18. B. Deo, R. Boom, *Fundamentals of Steelmaking Metallurgy* (Prentice-Hall, New York, NY, 1993)
19. S. Gosh, K. Margatan, A. Chong, J.-H. Bahk, Radiant heat recovery by thermoelectric generators: a theoretical case-study on hot steel casting. *Energy Convers. Manag.* **175**, 327–336 (2018)
20. S. Lineykin, S. Ben-yaakov, Modeling and analysis of thermoelectric modules. *IEEE Trans. Ind. Appl.* **43**(2), 505–512 (2007)
21. J.-H. Bahk, A. Abuhamdeh, K. Margatan, Solar thermoelectric module simulator [Online] (2018), <https://nanohub.org/tools/solarte>
22. Y. Hsiao, W. Chang and S. Chen, "A mathematic model of thermoelectric module with applications on waste heat recovery from automobile engine," *Energy*, vol. 35, no. 3, pp. 1447-1454, 2010
23. K. Yazawa, A. Shakouri, Cost-efficiency trade-off and the design of thermoelectric power generators. *Environ. Sci. Technol.* **45**, 7548–7553 (2011)
24. F. Kreith, R.M. Manglik, *Principles of Heat Transfer*, 8th edn. (Cengage, Boston, MA, 2018)
25. T.L. Bergman, A.S. Lavine, F.P. Incropera, D.P. DeWitt, *Fundamentals of Heat and Mass Transfer* (Wiley, Hoboken, NJ, 2017)
26. D. Kraemer, K. McEnaney, M. Chiesa, G. Chen, Modeling and optimization of solar thermoelectric generators for terrestrial applications. *Sol. Energy* **86**, 1338–1350 (2012)
27. G. Nolas, J. Sharp, J. Goldsmid, *Thermoelectrics Basic Principles and New Materials Developments* (Springer, New York, 2001)
28. C. Goupil (ed.), *Continuum Theory and Modeling of Thermoelectric Elements* (Wiley-VCH, Weinheim, 2016)
29. X. Yan, B. Poudel, Y. Ma, W.S. Liu, G. Joshi, H. Wang, Y. Lan, D. Wang, G. Chen, Z. Ren, Experimental studies on anisotropic thermoelectric properties and structures of n-type Bi₂Te_{2.7}Se_{0.3}. *Nano Lett.* **10**, 3373–3378 (2010)
30. B. Poudel, Q. Hao, Y. Ma, Y. Lan, A. Minnich, B. Yu, X. Yan, D. Wang, A. Muto, D. Vashaee, X. Chen, J. Liu, M.S. Dresselhaus, G. Chen, Z. Ren, High-thermoelectric performance of nanostructured bismuth antimony telluride bulk alloys. *Science* **320**, 634 (2008)
31. J.-W. Seo, Y.-H. Kim, D. Kim, Y.-D. Choi, K.-J. Lee, Heat transfer and pressure drop characteristics in straight microchannel of printed circuit heat exchangers. *Entropy* **17**, 3438 (2015)
32. J.-H. Bahk, A. Shakouri, Minority carrier blocking to enhance the thermoelectric figure of merit in narrow-band-gap semiconductors. *Phys. Rev. B* **93**, 165209 (2016)
33. F. Cao, D. Kraemer, T. Sun, Y. Lan, G. Chen, Z. Ren, Enhanced thermal stability of W-Ni-Al₂O₃ cermet-based spectrally selective solar absorbers with tungsten infrared reflectors. *Adv. Energy Mater.* **5**, 1401042 (2015)
34. H. Sadiq, M.B. Wong, J. Tashan, R. Al-Mahaidi, X.L. Zhao, Determination of steel emissivity for the temperature prediction of structural steel members in fire. *J. Mater. Civil. Eng.* **25**, 167–173 (2013)